Anisotropic bilinear magnetoresistance in (110) $SrTiO_3$-based two-dimensional electron gas

Jine Zhang,[1,*] Hui Zhang,[1,*] Xiaobing Chen,[2,3,*] Jing Zhang,[1,*] Shaojin Qi,[2,3] Furong Han,[2,3] Yuansha Chen,[2] Weisheng Zhao,[1,†] Fengxia Hu,[2,3,4] Baogen Shen,[2,3,4] and Jirong Sun[2,3,4,5,†]

[1]*School of Integrated Circuit Science and Engineering, Beihang University, Beijing 100191, People's Republic of China*
[2]*Beijing National Laboratory for Condensed Matter Physics & Institute of Physics, Chinese Academy of Sciences, Beijing 100190, People's Republic of China*
[3]*School of Physical Sciences, University of Chinese Academy of Sciences, Beijing 100049, People's Republic of China*
[4]*Songshan Lake Materials Laboratory, Dongguan, Guangdong 523808, People's Republic of China*
[5]*Spintronics Institute, University of Jinan, Jinan, Shandong 250022, People's Republic of China*

(Received 16 April 2021; revised 10 June 2021; accepted 28 June 2021; published 9 July 2021)

Bilinear magnetoresistance (BMR), the magnetoresistance that is linear against either magnetic field or applied current, is a hot topic of recent investigations. While most of the previous works focused on isotropic BMR, here we report on a strongly anisotropic BMR for (110) $SrTiO_3$-based two-dimensional electron gas (2DEG). Remarkably, the BMR measured along the [001] axis can be fivefold as large as that obtained along the [$1\bar{1}0$] axis. A close relation is found between BMR and current-induced effective Rashba field, and it is the anisotropy of the Rashba field that causes the anisotropic BMR. Based on the analysis of anisotropic magnetoresistance, effective Rashba fields up to 4.5 T are determined. The band structure of the 2DEG is further calculated, ellipse-shaped Fermi rings are obtained, and the respective effects of different Fermi rings on BMR are distinguished. This work demonstrates the great potential of anisotropic 2DEG for the exploration of unusual effects.

DOI: 10.1103/PhysRevB.104.045114

I. INTRODUCTION

Two-dimensional electron gas (2DEG) at the $LaAlO_3$/$SrTiO_3$ interface has attracted intensive attention since its discovery in 2004 by Hwang *et al.* [1], and diverse phenomena have been observed, including 2D superconductivity and its coexistence with interfacial ferromagnetism [2–5], gate tunable Rashba effect [6–9], spin-charge interconversion [10–16], and nonreciprocal conduction [17,18]. Among them, the latter two effects are particularly attractive in the sense that they provide opportunities to incorporate spin-orbitronic functionalities into 2DEG.

Due to Rashba spin-orbit coupling [19,20], the 2DEG confined at the $LaAlO_3$/$SrTiO_3$ interface exhibits an important feature, i.e., electron spin is constrained to lie in the direction perpendicular to the electron momentum in the film plane. Via this mechanism a nonequilibrium spin density can be converted into an electric current and vice versa, achieving spin-charge interconversion [11–16]. Also via this mechanism, an effective Rashba field can be produced by applying a DC electric current [21]. Particularly, spin-momentum locking can lead to unusual features marked by nonreciprocal resistive responses to applied DC currents [17,18]: The resistivity changes when reversing either the sign of the magnetic field or the polarity of the current. This feature underlies abundant physics and may provide an application to two-terminal spin-orbitronic devices.

Nonreciprocal resistance has been a focus of recent investigations, and it was widely observed in polar conductors/semiconductors [22–25], topological insulators [26,27] and bilayer structures composed of ferromagnetic film and heavy nonmagnetic film such as Pt/Co, Ta/Co, and Bi_2Se_3/CoFeB, etc. [28–30]. Unfortunately, the nonreciprocal coefficient (γ) of these systems are usually very small, in the order of 10^{-11}–10^{-8} A^{-1} T^{-1} cm^2 when normalized by applied magnetic field and electric current. Obviously, further efforts are still required to get materials with large γ.

2DEG at the oxide interface has characteristics that usually lead to unprecedented effects. Based on the analysis of the transport behavior with the character of weak antilocalization/localization, Caviglia *et al.* [6] deduced a large Rashba coefficient of $\sim 5 \times 10^{-12}$ eV m under gate biases, which is comparable to that of the typical semiconductor heterostructures [31]. By analyzing anisotropic magnetoresistance (AMR), Narayanapillai *et al.* [21] reported an effective Rashba field up to ~1.4 T when a strong current was applied to the 2DEG. As discussed above, the nonreciprocal resistance of 2DEG is induced by spin-momentum locking determined by Rashba spin-orbital coupling. A large Rashba coefficient implies a strong nonreciprocal charge transport. Indeed, strong nonreciprocity was recently reported for (001)-oriented 2DEG [18], exhibiting a nonreciprocal coefficient of $\gamma \sim 1.17 \times 10^{-7}$ A^{-1} T^{-1} cm^2 which is at least one order in magnitude more than previously reported values for other systems (10^{-11}–10^{-8} A^{-1} T^{-1} cm^2) [24–29]. Here we would like to emphasize an important feature of the nonreciprocal

*These authors contributed equally to this work.
†Corresponding authors: weisheng.zhao@buaa.edu.cn; jrsun@iphy.ac.cn

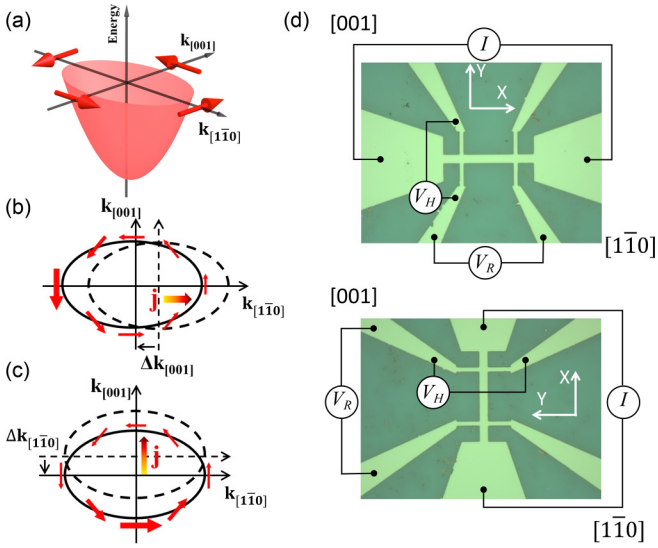

FIG. 1. A ketch of the Fermi surface and the devices adopted for present investigations. (a) A three-dimensional sketch of the energy dispersion relation of (110) 2DEG. Arrows mark the direction of electron spin. The long and short axes of the ellipse are explicitly marked. For clarity, only the dispersion relation with anti-clockwise spin chirality is shown. (b), (c) Ellipse- shaped Fermi contours. Dashed ellipse represents the Fermi contour in equilibrium state while solid ellipse is obtained after a shift against the direction of applied DC current. When deviating from equilibrium state, spin accumulation takes place as sketched by thick arrows. (d) Two photographs showing the representative Hall bars, along the [1$\bar{1}$0] and [001] axes of the elliptical Fermi contour, respectively. The Hall bar is 60 μm in length and 10 μm in width.

resistance of 2DEG, i.e., bilinear magnetoresistance (BMR); the magnetoresistance (MR) varies linearly against magnetic field or DC current.

We noted that the previous investigations focused on the (001)-oriented 2DEG, for which the Fermi contours form two concentric rings thus the spin-momentum locking is isotropic [14,15,17]. When the conducting interface has a normal direction deviating from [001], however, the Rashba spin-orbit coupling will be anisotropic, resulting in an effect with the features of direction dependence. This kind of 2DEG deserves special attention in the sense that it allows investigations of the hidden aspects of 2DEG. (110)-oriented 2DEG is a suitable system for this kind of investigation. It exhibits an elliptical Fermi contour at low carrier density [Fig. 1(a)] [32], along which the spin-momentum locking varies from location to location. Unfortunately, works on the effect of Rashba spin-orbit coupling of (110) 2DEG are scarce and the limited reports sometimes are inconsistent with each other [33,34]. Here we present a systematic investigation on (110) 2DEG, focusing on the distinct feature of anisotropic Rashba splitting and its effect. We observed strongly anisotropic bilinear magnetoresistance (BMR). It differs by a factor up to 5 when measured along different directions. A mapping of the BMR on the azimuth angle of the measuring direction is obtained, providing a complete description for anisotropic BMR. Thanks to spin-momentum locking, the applied current induces a strong effective Rashba field that makes the BMR anisotropic. Ellipse-shaped Fermi rings are theoretically predicted and the respective effects of different Fermi rings on BMR are identified.

II. EXPERIMENTAL DETAILS

Using the technique of pulsed laser deposition, a 2DEG sample was fabricated by growing a $(La_{0.3}Sr_{0.7})(Al_{0.65}Ta_{0.35})O_3$ (LSAT) film on a (110)-oriented $SrTiO_3$ (STO) single crystal substrate with a hard mask that defines four Hall bars (10 μm in width and 60 μm in length) with respectively the azimuth angles of 0°, 30°, 60°, and 90° with respect to the [1$\bar{1}$0] axis. The hard mask was prepared by depositing, at room temperature, an 80-nm-thick amorphous AlO_x film on a patterned STO by the conventional photolithographic technique and then removing the undesired part using a lift-off technique. The fluence of the laser pulse was 2 J/cm^2 and the repetition rate was 2 Hz (KrF excimer laser, wavelength = 248 nm). During deposition, the substrate temperature was maintained at 700 °C and the oxygen pressure was fixed to 5×10^{-5} mbar. After deposition, the sample was furnace cooled to room temperature without changing the oxygen pressure. The film thickness of LSAT was 6 nm, determined by the number of laser pulses that have been carefully calibrated by the technique of small angle x-ray reflectivity. For comparison investigations, two more samples were also fabricated by setting oxygen pressure to 4×10^{-5} and 1×10^{-5} mbar, respectively, with each having two Hall bars with the azimuth angles 0° and 90°. For simplicity, in the main text the samples will be named sample 1, sample 2, and sample 3, respectively.

Resistive measurements were conducted by a Quantum Design physical property measurement system (PPMS) in the temperature interval from 2 to 300 K and the magnetic field range from 0 to 7 T. An external sourcemeter (Keithley 2611B) and voltmeter (Keithley 2182A) were adopted. Ultrasonic wire bonding (Al wire of 20 μm in diameter) was used to get electric contacts. The standard four-probe geometry was employed. A DC current in the range 1–80 μA was applied for resistive measurements. To depress the effect of Joule heating, pulses of electric current with a width of 80 ms were adopted for resistive measurements.

III. RESULTS AND DISCUSSION

A. Anisotropic bilinear magnetoresistance

All three samples (sample 1, sample 2, and sample 3) are metallic in the temperature range 2–300 K, confirming the formation of 2DEGs confined to the (110) LSAT/STO interfaces. The carrier density (n_S) is, at 2 K, $\sim 1.6 \times 10^{13}$ cm^{-2} for sample 1, $\sim 1.8 \times 10^{13}$ cm^{-2} for sample 2, and $\sim 2.4 \times 10^{13}$ cm^{-2} for sample 3. As expected, a change in the orientation of the Hall bar does not affect carrier density. Hall mobility situates in the range $\sim$190–460 cm^2/V s at low temperatures. Please refer to Fig. S1 of the Supplemental Material [35] for detailed information.

For the 2DEGs investigated here, the level of band filling is relatively low. As a result, the Fermi surface exhibits a low symmetry, giving us opportunities to unveil hidden aspects of 2DEGs. Figure 1(a) is a three-dimensional sketch

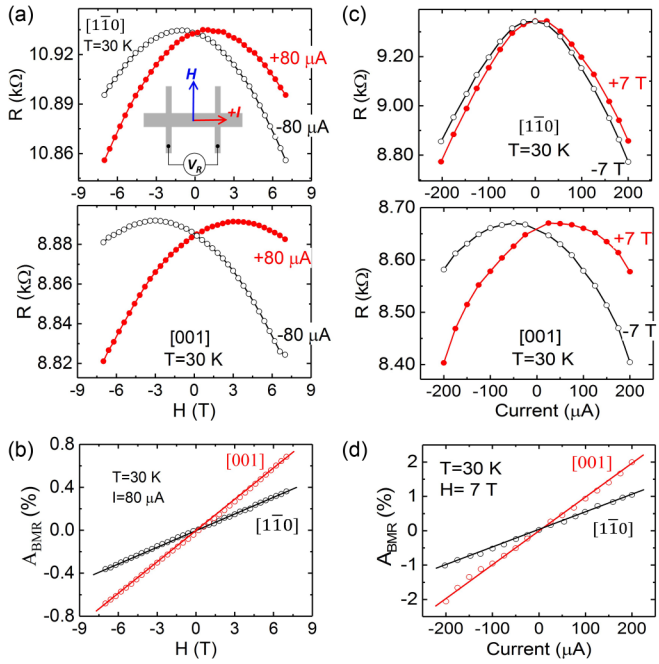

FIG. 2. (a) Sheet resistance as a function of magnetic field for Sample-1, recorded at 30 K along different the [1$\bar{1}$0] (upper panel) and [001] (bottom panel) axes. The applied current is 80 μA. Inset plot is a sketch for experimental setup. (b) Corresponding A_{BMR} which varies linearly with magnetic field. (c) Sheet resistance as a function of applied current, recorded at 30 K along the [1$\bar{1}$0] (upper panel) or [001] (bottom panel) axis. The applied magnetic field is 7 T. (d) Corresponding A_{BMR} which varies linearly with applied current. As expected, the MR is bilinear against magnetic field and applied current.

of the expected energy dispersion relation of (110) 2DEG. For clarity, only the most outside dispersion relation with anticlockwise spin helicity is shown. When the Fermi level is low enough, the constant-energy surface will be an ellipse with the feature of spin-momentum locking. Figures 1(b) and 1(c) show the ellipse-shaped Fermi contours (refer to Fig. 5 for practical Fermi contours). The dashed ellipse represents the Fermi contour in the equilibrium state. Upon the application of a DC current, the Fermi contour will shift against the direction of applied current, reaching a stable state marked by a solid ellipse. Simultaneously, spin accumulation takes place as indicated by thick arrows if significant Rashba spin splitting exists. From first glance, the spin accumulation will be different along the long and short axes of the elliptical Fermi contour for the same applied current. This implies a direction dependence of the current-induced Rashba effects, different from the (001) 2DEG that owns highly symmetric Fermi contours [14,15]. As an example, in Fig. 1(d) we show two photographs of Hall bars respectively along the [1$\bar{1}$0] and [001] axes of the elliptical Fermi contour for the investigation of orientation-dependent effect.

BMR is a distinct feature of the systems with spin-momentum locking. It is also observed in (110) 2DEG. Figure 2(a) shows the resistance (R_{xx}) as a function of magnetic field (H_y) for sample 1, where the resistance is measured along the x axis ($I_x = 80\,\mu$A) and magnetic field is applied along the y axis. The data in the top and bottom panels correspond to the current respectively along the [1$\bar{1}$0] and [001] directions. From first glance, the $R_{xx}(H_y)$ curve is strongly asymmetric, like an inclined dome. Reversing current polarity, the inclining direction reverses accordingly. The variation in the inclining direction implies a dependence on the current direction of the resistance of 2DEG. This is the so called nonreciprocal charge transport. In Fig. 2(b) we show the magnetic field dependence of the relative resistance change $A_{BMR} = [R_{xx}(H_y, +I_x) - R_{xx}(H_y, -I_x)]/2R_{xx}(0, I_x)$, caused by reversing current polarity ($I_x = 80\,\mu$A). A_{BMR} exhibits a good linear dependence on magnetic field. Notably, A_{BMR} is a special case of BMR, emerging when the in-plane applied current and magnetic field are orthogonal to each other.

Figures 2(c) and 2(d) illustrate the effect of applied current on MR and show a linear dependence of BMR on DC current ($H = 7$ T). According to Figs. 2(b) and 2(d), BMR is indeed bilinear against magnetic field or DC current. However, the A_{BMR}-H_y or the A_{BMR}-I_x slope is different along the [001] and the [1$\bar{1}$0] directions.

A further important character of the (110) 2DEG is the direction dependence of the nonreciprocal charge transport. Figure 3(a) shows the representative MR of different temperatures, defined by $[R_{xx}(H_y, I_x)\text{-}R_{xx}(0, I_x)]/R_{xx}(0, I_x)$, for sample 1 ($n_S = 1.6 \times 10^{13}\,\text{cm}^{-2}$), where $I_x = 80\,\mu$A is the DC current along the x axis. The data in the four panels correspond to the azimuth angles of 0°, 30°, 60°, and 90°, respectively. Notably, $\theta = 0°$ is the orientation of the [1$\bar{1}$0] axis and $\theta = 90°$ is the orientation of the [001] axis. The MR data for the other two samples can be found in Fig. S2 of the Supplementarl Material [35].

Compared with the isotropic nonreciprocal transport of (001) 2DEG (refer to Fig. S3 of the Supplementarl Material [35]), the nonreciprocal transport of (110) 2DEG exhibits a distinct feature: it strongly depends on the direction of resistance channels along which the resistive measurements have been conducted. This feature can be recognized by a direct comparison of the data in Fig. 3(a). From first glance, the BMR is considerably larger along the [001] axis ($\theta = 90°$) than along the [1$\bar{1}$0] axis ($\theta = 0°$), especially at low temperatures. For the other two azimuth angles of 30° and 60°, intermediate BMR values are obtained. A previous analysis [Figs. 2(b) and 2(c)] reveals a bilinear dependence of the BMR on magnetic field and applied current in differently directed Hall bars, indicating that the BMR generated by spin-momentum locking through Fermi contour now is anisotropic. With the increase of temperature, the BMR decreases and, simultaneously, its direction dependence weakens.

In Fig. 3(b) we show A_{BMR} as a function of T for all three samples with different carrier densities. As expected, temperature has a strong effect on nonreciprocal transport. At temperatures above 70 K, the A_{BMR}-T curves collected along different directions overlap with each other, indicating the absence of direction dependence. This can be ascribed to the effect of thermal spin fluctuation, which disturbs the spin-momentum locking. As reported, the Rashba spin-splitting energy of 2DEG is ~35 K [6,36]. Thermal effect will be strong well above this character temperature. With the decrease of temperature, the A_{BMR}-T curves depart from each other rapidly and, meanwhile, A_{BMR} undergoes a dramatic

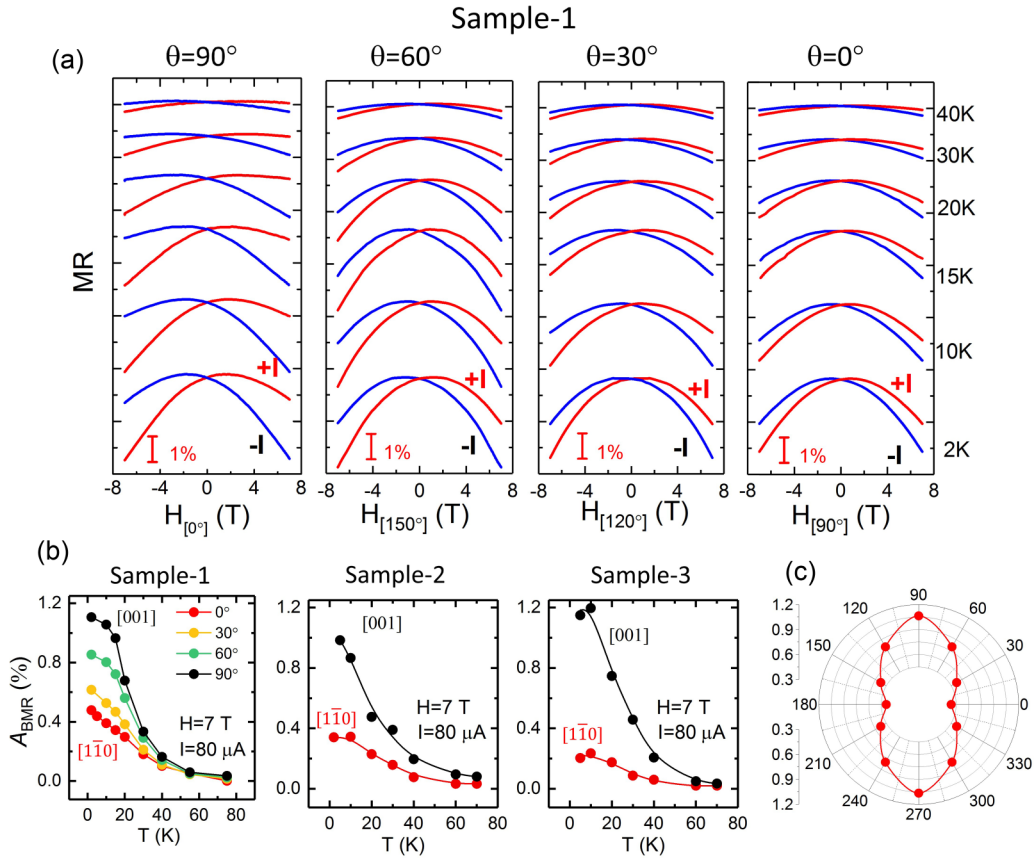

FIG. 3. Anisotropic BMR. (a) Magnetoresistance as a function of magnetic field for Sample-1, recorded at different temperatures. The four panels corresponding to the azimuth angles of 0°, 30°, 60°, and 90° of the Hall bars, respectively. For clarity, curves were upwards shifted with the increase of temperature. The applied current is 80 μA. Labels in the figure mark the direction of applied current. Positive current flows along the x-axis in Fig. 1(d). (b) Temperature dependence of A_{BMR}. Direction dependence of the A_{BMR} is observed in all samples investigated. (c) A_{BMR} values as functions of azimuth angle for Sample-1. A cucurbit-shaped curve is obtained, clearly demonstrating anisotropic BMR.

growth. Take sample 1 as an example. $A_{\mathrm{BMR}}[001]$ increases from ~0.15% at 40 K to ~1.15% at 2 K and $A_{\mathrm{BMR}}[1\bar{1}0]$ from ~0.12% to ~0.5%, where the orientation ([001] or [1$\bar{1}$0]) denotes the axis along which A_{BMR} is determined. The corresponding $A_{\mathrm{BMR}}[001]/A_{\mathrm{BMR}}[1\bar{1}0]$ ratio is ~1.2 at 40 K and ~2.3 at 2 K: obviously, BMR shows strongly anisotropic. Anisotropic BMR seems to be a general feature of the (110) 2DEGs, also observed in sample 2 and sample 3 [Fig. 3(b)]. It is noteworthy that the degree of anisotropy is carrier density dependent. As n_{S} grows from $\sim 1.6 \times 10^{13}\,\mathrm{cm}^{-2}$ to $\sim 2.4 \times 10^{13}\,\mathrm{cm}^{-2}$, the $A_{\mathrm{BMR}}[001]/A_{\mathrm{BMR}}[1\bar{1}0]$ ratio increases from ~2.3 to ~5.1 ($T = 2$ K). $A_{\mathrm{BMR}}[001]/A_{\mathrm{BMR}}[1\bar{1}0] = 5.1$ is a strong anisotropy that is obviously larger than the long to short axis ratio of the Fermi contours [Figs. 1(b) and 1(c)]. As will be shown later, this is a consequence of the change in the structure of the Fermi contours. To compare the strength of BMR with previously reported results of different systems, we define a figure of merit $\gamma = A_{\mathrm{BMR}}/H_{\mathrm{Y}}J_{\mathrm{X}}$, adopting the thickness of 2DEG of 7 nm [37], where $J_{\mathrm{X}} = I_{\mathrm{X}}/S$ is the current density (S is the cross-sectional area of the Hall bar). The maximum γ for (110) 2DEG is as high as $\sim 1.47 \times 10^{-8}\,\mathrm{A}^{-1}\,\mathrm{T}^{-1}\,\mathrm{cm}^2$. This value is much larger than that of other typical systems, such as a-GeTe ($\gamma \sim 1 \times 10^{-11}\,\mathrm{A}^{-1}\,\mathrm{T}^{-1}\,\mathrm{cm}^2$) [25], Bi_2Se_3 ($\gamma \sim 2 \times 10^{-11}\,\mathrm{A}^{-1}\,\mathrm{T}^{-1}\,\mathrm{cm}^2$) [27], and Bi_2Se_3/CoFeB bilayers ($\gamma \sim 1.02 \times 10^{-9}\,\mathrm{A}^{-1}\,\mathrm{T}^{-1}\,\mathrm{cm}^2$) [28]. If our 2DEGs are treated as two-dimensional systems, the unit of current density will be A/m. The corresponding γ values in this case were presented in Fig. S4 of the Supplementarl Material [35] for reference.

For sample 1, we also investigated the BMR along two intermediate azimuth angles 30° and 60°, and obtained A_{BMR} values between $A_{\mathrm{BMR}}[1\bar{1}0]$ and $A_{\mathrm{BMR}}[001]$. Figure 3(c) presents the A_{BMR} values as a function of azimuth angle of the resistance channel, where the data in the second, third, and four quadrants are the symmetric images of those in the first quadrant. A cucurbit-shaped $A_{\mathrm{BMR}} \sim \theta$ curve is obtained, with a [001]-directed long axis and a [1$\bar{1}$0]-directed short axis. Superficially, these results are consistent with the expectations of the sketch in Fig. 1.

B. Rashba fields induced by the current flowing along different directions

A primary explanation for the nonreciprocal transport of noncentrosymmetric systems is as follows [17,26,38]: When a current is applied to the resistance channel of the 2DEG, an electric field is established. It in turn results in a spin accumulation via the Edelstein mechanism, yielding an effective Rashba field (H_{R}). In principle, H_{R} is constrained in the film plane and perpendicular to the direction of applied current.

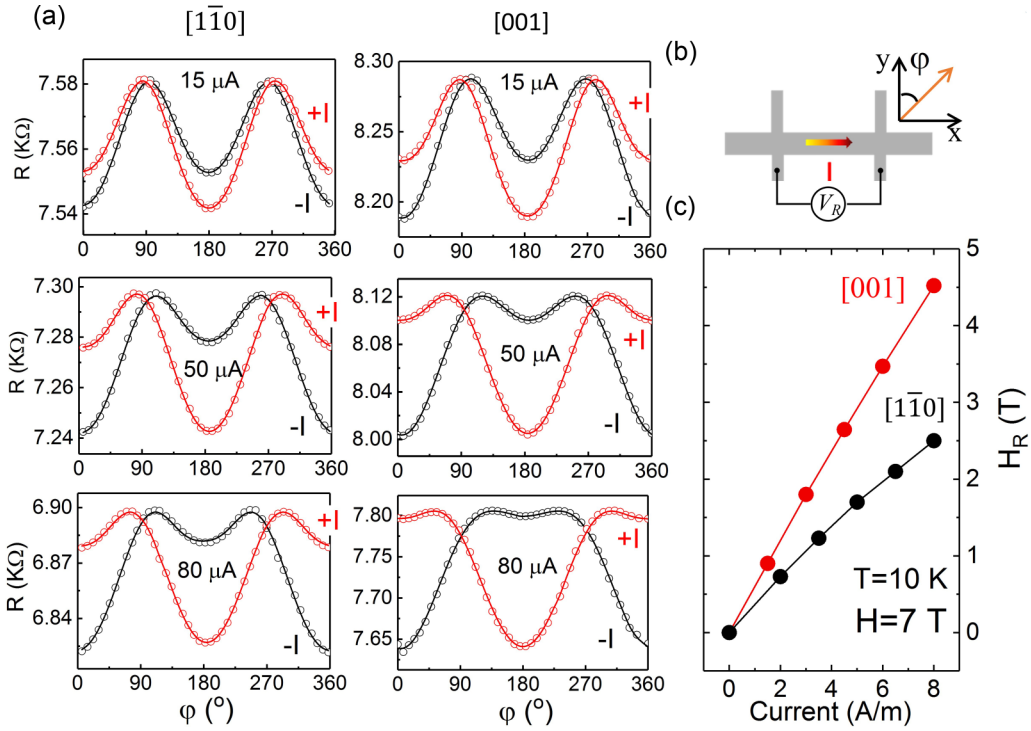

FIG. 4. Anisotropic magnetoresistance and extracted effective Rashba field. (a) Anisotropic magnetoresistance measured at 10 K while rotating applied field in film plane ($H = 7$ T). The experiment curve is of asymmetry that develops with applied current. Symbols are experiment data and solid lines are the results of curve fitting based on Eq. (1). (b) A sketch of the experiment setup. (c) Effective Rashba field as a function of electric current. It increases nearly linearly with applied current. Labels in the figure denote the direction of applied current. All data are for Sample-1.

If the current is applied in such a manner that it produces a Rashba field parallel to external magnetic field (H_A), the MR effect will be enhanced. Reversing the current direction will reverse the direction of the Rashba field. Accordingly, the MR effect is weakened. The difference of these two MR effects defines the BMR. The orientation dependence of the BMR is intriguing. It implies that the Rashba field will be different if the current is applied along the resistance channels with different azimuth angles.

To get a quantitative description for the Rashba field, we performed a further investigation on AMR. Since AMR is jointly determined by external magnetic field and effective Rashba field, we can get direct information on H_R from the results of AMR. Figure 4(a) illustrates the AMR as a function of the angle (φ) between magnetic field and the y axis [as sketched in Fig. 4(b)], collected at 10 K for the representative sample (sample 1). The left and right columns present the results corresponding to the current along the [1$\bar{1}$0] and [001] directions, respectively. The magnetic field is fixed to 7 T and the applied current varies from 15 to 80 μA. The most remarkable feature of the AMR is the systematic variation of two local minima at $\varphi = 0°(360°)$ and $\varphi = 180°$, respectively: With the increase of positive current, the second minimum becomes deeper and deeper at the expense of the first one. Reversing the current direction, the evolution process of the local minima reverses. This is a general feature of the present AMR, observed at different temperatures (refer to Supplemental Material Fig. S5) [35]. It is an indication for the presence of an in-plane effective Rashba field, perpendicular to the current direction. Based on the equation [21]

$$R_{XX} = a_0 + a_1 H_{\text{eff}}^2 \cos^2(\varphi - \alpha) + a_2 H_{\text{eff}}^2 \cos^4(\varphi - \alpha), \quad (1)$$

the experimental results have been well reproduced (the symbols are experiment data and the solid lines are the results of curve fitting) adopting appropriate fitting parameters a_0, a_1, a_2, and H_R, where H_{eff} is an effective field that is expressed by H_A (applied magnetic field) and H_R via the relation

$$H_{\text{eff}}^2 = H_A^2 + H_R^2 + 2H_A H_R \cos\varphi,$$

and

$$\alpha = \arctan[H_R \sin\varphi / (H_A + H_R \cos\varphi)].$$

The deduced Rashba field is shown in Fig. 4(c). The most remarkable observation is that for the same current the resultant Rashba field is considerably different when the current is applied along different directions. Corresponding to the DC current of 80 μA, for example, the H_R is 4.5 T when the current flows along the [001] direction and 2.5 T for the current along [1$\bar{1}$0]. The former is larger than the latter by a factor of ~1.8. Obviously, the BMR should be larger along the [001] direction than along the [1$\bar{1}$0] direction, exhibiting anisotropic behavior. Notably, We can define a new quantity $A_{\text{QMR}} = \text{QMR}(\varphi = 90°) - \text{QMR}(\varphi = 0°)$, where $\text{QMR} = [\text{MR}(H, +I_x) + \text{MR}(H, -I_x)]/2$ (H is an in-plane field). Take the results of the typical condition ($T = 10$ K, $H = 7$ T, $I = 80\,\mu$A) in Fig. 4(a) as examples. The $A_{\text{BMR}}/A_{\text{QMR}}$ ratio equals 1.31 along the [001] direction and 0.65 along the [1$\bar{1}$0] direction. For an isotropic system, the

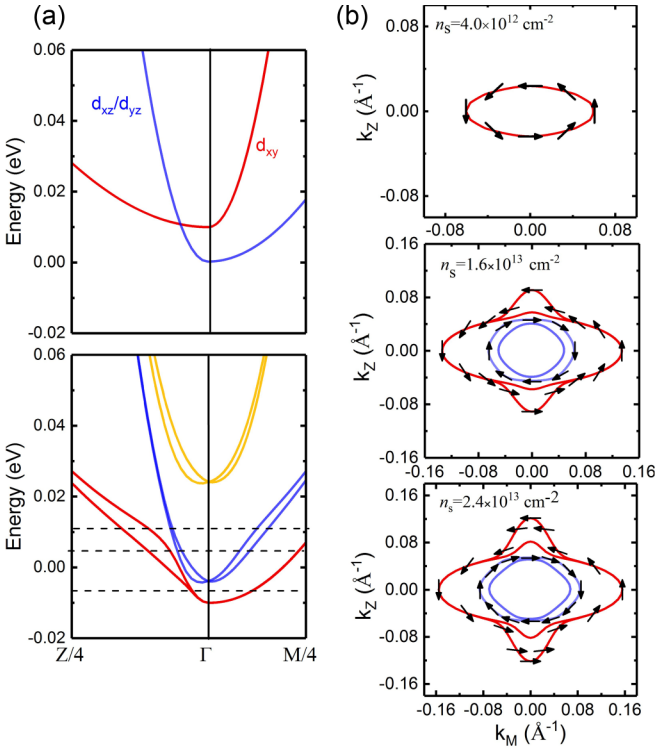

FIG. 5. Electronic band structure. (a) Energy dispersion relation of the surface state of (110) STO, without (upper panel) and with (bottom panel) inter band hybridization caused by spin-orbit interaction. Based on (a), Rashba spin-splitting energy can be estimated. Dashed lines mark the positions of Fermi levels. (b) Fermi contours corresponding to the three Fermi levels in (a). Where M corresponds to [1$\bar{1}$0], and Z to [001]. Labels in the figure mark the corresponding carrier density. The Fermi contours are complex, composed of outside and inside Fermi rings. For clarity, only anti-clockwise (clockwise) spin helicity is shown for the outside (inside) Fermi contours.

Rashba coefficient α_R can be deduced from the A_{BMR}/A_{QMR} ratio [17]. For anisotropic systems like (110) 2DEGs, unfortunately, the relation between A_{BMR}/A_{QMR} and α_R is not clear at present.

C. Low symmetric Fermi contours and its effects on BMR

To get a deep understanding of the anisotropic BMR, we modeled the band structure of (110) $SrTiO_3$-based interface supplemented by atomic spin-orbit interactions and an interorbital hopping induced by the interface asymmetry. Detailed information about the tight-binding Hamiltonian for multiband systems is given in Note 1 of the Supplemental Material [35]. Figure 5(a) shows the electronic band structure of (110) 2DEG. Without spin-orbit coupling, two branches of energy dispersion relations with twofold and fourfold degeneracy, respectively, are obtained [upper panel of Fig. 5(a)]. However, spin-orbit interaction splits the degenerated d_{xz}/d_{yz} and d_{xy} orbitals, resulting in six branches of dispersion relations with sizable Rashba spin splitting along the Γ-Z direction near the Γ point [bottom panel of Fig. 5(a)]. Cutting the three-dimensional dispersion relations with slices at different energy levels, we get a series of Fermi surfaces, corresponding to different degrees of band filling [Fig. 5(b)]. When band filling is low, an elliptic Fermi contour is obtained, without visible spin splitting. With the increase of Fermi level, the Fermi contour remains essentially elliptic. However, a hump Fermi arc emerges across the k_Z axis, above the elliptic base line. Meanwhile, two inside Fermi rings exhibiting opposite spin helicity appear. A further calculation indicates that about 75% of charge carriers are accommodated by the energy bands corresponding to the outside Fermi contours, and the remaining charge carriers occupied the energy bands of the inside Fermi rings. The samples investigated here own the Fermi contours shown in the middle and bottom panels of Fig. 5(b). In this case, the outside Fermi arc that crosses the k_M axis exhibits a very small Rashba spin splitting (∼20 μeV). In contrast, the spin-splitting energy of the Fermi arc cross the k_Z axis is as high as ∼2.2 meV ($n_S = 1.6 \times 10^{13}$ cm^{-2}) or ∼6.0 meV ($n_S = 2.4 \times 10^{13}$ cm^{-2}), thanks to the formation of hump-shaped Fermi arc.

Based on these data, we can figure out the correspondence between the BMR and the structure features of the Fermi surface. The outside Fermi contour should be responsible for the nonreciprocal transport along the [001] axis (corresponding to the k_Z axis) since it owns a large Rashba spin-splitting energy and a high carrier population. A current flowing in this direction will generate a large effective Rashba field, leading to a strong BMR. Along the [1$\bar{1}$0] direction (corresponding to the k_M axis), however, the BMR may be produced by the inside Fermi rings, which exhibit a sizable spin splitting (∼1.0 meV for $n_S = 1.6 \times 10^{13}$ cm^{-2} and ∼3.2 meV for $n_S = 2.4 \times 10^{13}$ cm^{-2}) that is large enough to cause a visible nonreciprocal conduction. As for the outside Fermi contour, its Rashba spin-splitting energy is too small (20 μeV) to produce any detectable effects. Notably, the difference of the spin-splitting energy along the [001] and [1$\bar{1}$0] axes is the largest for sample 3 (6.0 vs 3.2 meV). This explains why this sample exhibits the strongest anisotropic BMR [$A_{BMR}[001]/A_{BMR}[1\bar{1}0] = 5.1$, Fig. 3(b)]. Obviously, the detailed feature of the Fermi contours is crucially important; it determines the details of the spin-momentum locking thus the details of the BMR.

D. DISCUSSION

Although (110) 2DEG has been intensively studied before, most of those works focused on the conventional transport properties [34,39,40] and the effects associated with spin-momentum locking have been less concerned. Due to low symmetry, as demonstrated above, (110) 2DEG exhibits complex Fermi contours that are absent in symmetric (001) 2DEG. This will allow an investigation of the hidden aspects of the 2DEG. For example, the present work reveals the different roles of the outside and inside Fermi rings: The outside Fermi contour supports an anisotropic BMR while the inside Fermi favors an isotropic BMR in the n_S range investigated here. Applying current along different directions invokes different parts of the Fermi contours, causing different BMR.

The kernel mechanism underlying the BMR is spin-momentum locking [17,26,38]. This mechanism converts the applied current into spin accumulation, leading to Rashba

field and thus BMR. Due to the low symmetric Fermi contours, the efficiency for the charge-to-spin conversion is current direction dependent. Also via spin-momentum locking, a reverse process, i.e., spin-to-charge conversion, will be achieved by injecting spin current into the 2DEG using, for example, spin pumping. In this case, the conversion efficiency could be also anisotropic thanks to the low symmetry of the Fermi contours of (110) 2DEG. However, now it will be magnetic direction rather than current direction dependent.

A further remarkable observation is the high conversion efficiency from electric current to Rashba field. As reported, for (001) 2DEG a current density of $\sim 8.9 \times 10^9$ A/m^2 can produce a Rashba field of $\sim$1.3 T [21]. For the (110) 2DEG, in contrast, a Rashba field of 4.5 T (along the [001] direction) only requires a current density of 1.1×10^9 A/m^2, assuming a thickness of 7 nm for the 2DEG as early reported [37]. The conversion efficiency has been about 36-fold enhanced from (001) 2DEG to (110) 2DEG. Even along the [1$\bar{1}$0] axis of the (110) 2DEG, along which the Rashba field is relatively low (2.5 T), the enhancement of the conversion efficiency is still about 20-fold. The underlying reason is still not clear at present. Presumably, (110) STO owns a polar surface, different from the (001) STO surface.

Finally, we would like to emphasize that the thermal effect in the present work is unimportant, and no special attention has been paid to it. In fact, we have measured the Nernst effect [38] and found that its contribution is at most 5% of the total signals (see Supplemental Material Fig. S6) [35].

IV. CONCLUSION

In summary, nonreciprocal charge transport characterized by BMR has been investigated for the (110) 2DEGs with low symmetry Fermi surfaces. The BMR is highly anisotropic, altering by a factor up to 5 while applying current along the long and short axes of the elliptic Fermi contours. Current-induced effective Rashba field is determined. Its variation from parallel to antiparallel to external magnetic field causes the BMR. The band structure of the 2DEG is calculated, and correlations between the detailed features of the BMR and the Fermi contour are identified. The present work uncovers the unknown aspects of anisotropic 2DEG, opening new space for further explorations.

ACKNOWLEDGMENTS

This work has been supported by the Science Center of the National Science Foundation of China (Grant No. 52088101), the National Key R&D Program of China (Grants No. 2016YFA0300701, No. 2017YFA0303601, No. 2017YFA0206300, No. 2018YFA0305704, No. 2019YFA0308401, and No. 2019YFA0704904), the National Natural Science Foundation of China (Grants No. 11934016, No. 12004022, No. 51972335, and No. 51590880), and the Key Program of the Chinese Academy of Sciences. J.R.S. is thankful for the support of the Project for Innovative Research Team of National Natural Science Foundation of China (Project No. 11921004).

[1] A. Ohtomo and H. Y. Hwang, Nature (London) **427**, 423 (2004).
[2] J. A. Bert, B. Kalisky, C. Bell, M. Kim, Y. Hikita, H. Y. Hwang, and K. A. Moler, Nat. Phys. **7**, 767 (2011).
[3] L. Li, C. Richter, J. Mannhart, and R. C. Ashoori, Nat. Phys. **7**, 762 (2011).
[4] D. A. Dikin, M. Mehta, C. W. Bark, C. M. Folkman, C. B. Eom, and V. Chandrasekhar, Phys. Rev. Lett. **107**, 056802 (2011).
[5] D. Stornaiuolo, C. Cantoni, G. M. DeLuca, R. Di Capua. E. Di Gennaro, G. Ghiringhelli, B. Jouault, D. Marre, D. Massarotti, F. M. Granozio, I. Pallecchi, C. Piamonteze, S. Rusponi, F. Tafuri, and M. Salluzzo, Nat. Mater. **15**, 278 (2016).
[6] A. D. Caviglia, M. Gabay, S. Gariglio, N. Reyren, C. Cancellieri, and J. M. Triscone, Phys. Rev. Lett. **104**, 126803 (2010).
[7] W. Niu, Y. Zhang, Y. L. Gan, D. V. Christensen, M. V. Soosten, E. J. Garcia-Suarez, A. Riisager, X. F. Wang, Y. B. Xu, R. Zhang, N. Pryds, and Y. Z. Chen, Nano Lett. **17**, 6878 (2017).
[8] M. Diez, A. M. R. V. L. Monteiro, G. Mattoni, E. Cobanera, T. Hyart, E. Mulazimoglu, N. Bovenzi, C. W. J. Beenakker, and A. D. Caviglia, Phys. Rev. Lett. **115**, 016803 (2015).
[9] M. Ben Shalom, M. Sachs, D. Rakhmilevitch, A. Palevski, and Y. Dagan, Phys. Rev. Lett. **104**, 126802 (2010).
[10] H. R. Zhang, Y. Ma, H. Zhang, X. B. Chen, S. H. Wang, G. Li, Y. Yun, X. Yan, Y. S. Chen, F. X. Hu, J. W. Cai, B. G. Shen, W. Han, and J. R. Sun, Nano Lett. **19**, 1605 (2019).
[11] Q. Song, H. R. Zhang, T. Su, W. Yuan, Y. Chen, W. Xing, J. Shi, J. R. Sun, and W. Han, Sci. Adv. **3**, e1602312 (2017).
[12] Y. Wang, R. Ramaswamy, M. Motapothula, K. Narayanapillai, D. P. Zhu, J. W. Yu, T. Venkatesan, and H. Yang, Nano Lett. **17**, 7659 (2017).
[13] D. C. Vaz, P. Noël, A. Johansson, B. Göbel, F. Y. Bruno, G. Singh, S. McKeown-Walker, F. Trier, L. M. Vicente-Arche, A. Sander, S. Valencia, P. Bruneel, M. Vivek, M. Gabay, N. Bergeal, F. Baumberger, H. Okuno, A. Barthélémy, A. Fert, L. Vila *et al.*, Nat. Mater. **18**, 1187 (2019).
[14] E. Lesne, Y. Fu, S. Oyarzun, J. C. Rojas-Sanchez, D. C. Vaz, H. Naganuma, G. Sicoli, J. P. Attane, M. Jamet, E. Jacquet, J. M. George, A. Barthelemy, H. Jaffres, A. Fert, M. Bibes, and L. Vila, Nat. Mater. **15**, 1261 (2016).
[15] P. Noël, F. Trier, L. V. M. Arche, J. Brehin, D. C. Vaz, V. Garcia, S. Fusil, A. Barthelemy, L. Vila, M. Bibes, and J. P. Attane, Nature (London) **580**, 483 (2020).
[16] F. Trier, D. C. Vaz, P. Bruneel, P. Noël, A. Fert, L. Vila, J.-P. Attané, A. Barthélémy, M. Gabay, H. Jaffrès, and M. Bibes, Nano Lett. **20**, 395 (2020).
[17] D. C. Vaz, F. Trier, A. Dyrdał, A. Johansson, K. Garcia, A. Barthélémy, I. Mertig, J. Barnaś, A. Fert, and M. Bibes, Phys. Rev. Mater. **4**, 071001(R) (2020).
[18] D. Choe, M. J. Jin, S.-I. Kim, H.-J. Choi, J. Jo, I. Oh, J. Park, H. Jin, H. C. Koo, B.-C. Min, S. Hong, H.-W. Lee, S.-H. Baek, and J.-W. Yoo, Nat. Commun. **10**, 4510 (2019).
[19] A. Manchon, H. C. Koo, J. Nitta, S. M. Frolov, and R. A. Duine, Nat. Mater. **14**, 871 (2015).
[20] J. Varignon, L. Vila, A. Barthélémy, and M. Bibes, Nat. Phys. **14**, 322 (2018).

[21] K. Narayanapillai, K. Gopinadhan, X. P. Qiu, A. Annadi, T. Venkatesan Ariando, and H. Yang, Appl. Phys. Lett. **105**, 162405 (2014).
[22] G. L. J. A. Rikken and P. Wyder, Phys. Rev. Lett. **94**, 016601 (2005).
[23] F. Pop, P. Auban-Senzier, E. Canadell, G. L. J. A. Rikken, and N. Avarvari, Nat. Commun. **5**, 3757 (2014).
[24] T. Ideue, K. Hamamoto, S. Koshikawa, M. Ezawa, S. Shimizu, Y. Kaneko, Y. Tokura, N. Nagaosa, and Y. Iwasa, Nat. Phys. **13**, 578 (2017).
[25] Y. Li, Y. Li, P. Li, B. Fang, X. Yang, Y. Wen, D. X. Zheng, C. H. Zhang, X. He, A. Manchon, Z. H. Cheng, and X. X. Zhang, Nat. Commun. **12**, 540 (2021).
[26] A. Dyrdał, J. Barnaś, and A. Fert, Phys. Rev. Lett. **124**, 046802 (2020).
[27] P. He, S. S. L. Zhang, D. P. Zhu, Y. Liu, Y. Wang, J. W. Yu, G. Vignale, and H. Yang, Nat. Phys. **14**, 495 (2018).
[28] Y. Lv, J. Kally, D. L. Zhang, J. S. Lee, M. Jamali, N. Samarth, and J. P. Wang, Nat. Commun. **9**, 111 (2018).
[29] C. O. Avci, K. Garello, A. Ghosh, M. Gabureac, S. F. Alvarado, and P. Gambardella, Nat. Phys. **11**, 570 (2015).
[30] S. S.-L. Zhang and G. Vignale, Phys. Rev. B **94**, 140411(R) (2016).
[31] G. Engels, J. Lange, Th. Schäpers, and H. Lüth, Phys. Rev. B **55**, R1958 (1997).
[32] Z. M. Wang, Z. C. Zhong, X. F. Hao, S. Gerhold, B. Stoger, M. Schmid, J. Sanchez-Barriga, A.Varykhalov, C. Franchini, K. Held, and U. Diebold, Proc. Natl. Acad. Sci. USA **111**, 3933 (2014).
[33] K. Gopinadhan, A. Annadi, Y. Kim, A. Srivastava, B. Kumar, J. Chen, J. M. D. Coey, A. Ariando, and T. Venkatesan, Adv. Electron. Mater. **1**, 1500114 (2015).
[34] G. Herranz, G. Singh, N. Bergeal, A. Jouan, J. Lesueur, J. Gazquez, M. Varela, M. Scigaj, N. Dix, F. Sanchez, and J. Fontcuberta, Nat. Commun. **6**, 6028 (2015).
[35] See Supplemental Material at http://link.aps.org/supplemental/10.1103/PhysRevB.104.045114 for details of samples about the basic properties, bilinear magnetoresistance, nonreciprocal coefficient (γ) as functions of temperature and azimuth angle, the effect of thermal effect, and the tight-binding three bands model.
[36] K. V. Shanavas, Z. S. Popović, and S. Satpathy, Phys. Rev. B **90**, 165108 (2014).
[37] M. Basletic, J.-L. Maurice, C. Carrétéro, G. Herranz, O. Copie, M. Bibes, É. Jacquet, K. Bouzehouane, S. Fusil, and A. Barthélémy, Nat. Mater. **7**, 621 (2008).
[38] T. Guillet, C. Zucchetti, Q. Barbedienne, A. Marty, G. Isella, L. Cagnon, C. Vergnaud, H. Jaffrès, N. Reyren, J.-M. George, A. Fert, and M. Jamet, Phys. Rev. Lett. **124**, 027201 (2020).
[39] A. Annadi, Q. Zhang, X. Renshaw Wang, N. Tuzla, K. Gopinadhan1, W. M. Lü, A. Roy Barman, Z. Q. Liu, A. Srivastava, S. Saha, Y. L. Zhao, S. W. Zeng, S. Dhar, E. Olsson, B. Gu, S. Yunoki, S. Maekawa, H. Hilgenkamp, T. Venkatesan, and Ariando, Nat. Commun. **4**, 1838 (2013).
[40] Z. Q. Liu, C. J. Li, W. M. Lü, X. H. Huang, Z. Huang, S. W. Zeng, X. P. Qiu, L. S. Huang, A. Annadi, J. S. Chen, J. M. D. Coey, T. Venkatesan, and Ariando, Phys. Rev. X **3**, 021010 (2013).